

Solid-source metal–organic molecular beam epitaxy of epitaxial RuO₂ ^{EP}

Cite as: APL Mater. **9**, 091112 (2021); <https://doi.org/10.1063/5.0062726>

Submitted: 07 July 2021 • Accepted: 23 August 2021 • Published Online: 23 September 2021

William Nunn,  Sreejith Nair, Hwanhui Yun, et al.

COLLECTIONS

 This paper was selected as an Editor's Pick



View Online



Export Citation



CrossMark

ARTICLES YOU MAY BE INTERESTED IN

[Spintronic terahertz emitters: Status and prospects from a materials perspective](#)

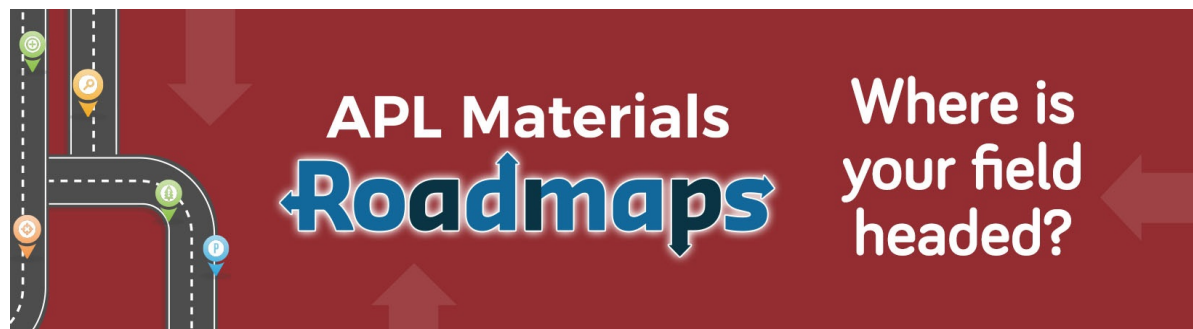
APL Materials **9**, 090701 (2021); <https://doi.org/10.1063/5.0057511>

[Synthesis science of SrRuO₃ and CaRuO₃ epitaxial films with high residual resistivity ratios](#)

APL Materials **6**, 046101 (2018); <https://doi.org/10.1063/1.5023477>

[Hybrid molecular beam epitaxy growth of BaTiO₃ films](#)

Journal of Vacuum Science & Technology A **39**, 040404 (2021); <https://doi.org/10.1116/6.0001140>



APL Materials
Roadmaps

Where is your field headed?

Solid-source metal-organic molecular beam epitaxy of epitaxial RuO₂

Cite as: APL Mater. 9, 091112 (2021); doi: 10.1063/5.0062726

Submitted: 7 July 2021 • Accepted: 23 August 2021 •

Published Online: 23 September 2021



View Online



Export Citation



CrossMark

William Nunn, Sreejith Nair,  Hwanhui Yun, Anusha Kamath Manjeshwar,  Anil Rajapitamahuni, Dooyong Lee,  K. Andre Mkhoyan,  and Bharat Jalan^{a)} 

AFFILIATIONS

Department of Chemical Engineering and Materials Science, University of Minnesota, Minneapolis, Minnesota 55455, USA

^{a)} Author to whom correspondence should be addressed: bjalan@umn.edu

ABSTRACT

A seemingly simple oxide with a rutile structure, RuO₂, has been shown to possess several intriguing properties ranging from strain-stabilized superconductivity to a strong catalytic activity. Much interest has arisen surrounding the controlled synthesis of RuO₂ films, but unfortunately, utilizing atomically controlled deposition techniques, such as molecular beam epitaxy (MBE), has been difficult due to the ultra-low vapor pressure and low oxidation potential of Ru. Here, we demonstrate the growth of epitaxial, single crystalline RuO₂ films on different substrate orientations using the novel solid-source metal-organic (MO) MBE. This approach circumvents these issues by supplying Ru using a “pre-oxidized” solid MO precursor containing Ru. High-quality epitaxial RuO₂ films with a bulk-like room-temperature resistivity of 55 $\mu\Omega$ cm were obtained at a substrate temperature as low as 300 °C. By combining x-ray diffraction, transmission electron microscopy, and electrical measurements, we discuss the effect of substrate temperature, orientation, film thickness, and strain on the structure and electrical properties of these films. Our results illustrating the use of a novel solid-source metal-organic MBE approach pave the way to the atomic-layer controlled synthesis of complex oxides of “stubborn” metals, which are not only difficult to evaporate but also hard to oxidize.

© 2021 Author(s). All article content, except where otherwise noted, is licensed under a Creative Commons Attribution (CC BY) license (<http://creativecommons.org/licenses/by/4.0/>). <https://doi.org/10.1063/5.0062726>

I. INTRODUCTION

RuO₂ has gained considerable attention for the rich material properties it exhibits. High thermal conductivity, strong resistance to chemicals, and high electrical conductivity resulted in RuO₂ being used historically in thermometers,¹ integrated circuits,² plasmonic applications³ and as electrodes in supercapacitors.^{4,5} RuO₂ also shows excellent catalytic properties, for example, being a highly active oxygen evolution reaction catalyst.^{6,7} When alloyed with metals such as La, RuO₂ exhibits a decrease in thermal conductivity and therefore has been argued to be potentially useful in thermoelectric devices.^{8,9} More recently, several novel phenomena have also emerged in RuO₂ films, such as itinerant antiferromagnetism and strain-stabilized superconductivity (Fig. 1).^{10,11} Additionally, RuO₂ also serves as a precursor to the growth of more complex materials, such as perovskite SrRuO₃ and Sr₂RuO₄, which are shown to exhibit itinerant ferromagnetism and unconventional superconductivity, respectively.

Bulk RuO₂ stabilizes in the prototypical tetragonal rutile crystal structure (Fig. 1) with space group No. 136, $P4_2/mnm$, and with lattice parameters $a = b = 4.492$ Å and $c = 3.106$ Å.¹² For thin films, RuO₂ has mostly been prepared as polycrystalline films^{13–17} although recently several papers on epitaxial crystalline films have been reported.^{10,11,18–24} Molecular beam epitaxy (MBE) is one of these thin film techniques that have been used for the growth of epitaxial single crystalline RuO₂.^{10,11,18–20} In general, the growth of Ru-based oxides in oxide MBE is challenging due to the ultra-low vapor pressure and low oxidation potential of Ru. Temperatures exceeding 2000 °C are needed to achieve a suitable Ru vapor pressure for growth, which is why reports of MBE-grown RuO₂ have all used electron-beam (e-beam) evaporators. Furthermore, the low oxidation potential makes stabilizing the Ru⁴⁺ in RuO₂ difficult and has led to ozone, a highly oxidizing source, being the preferred oxidant in most reports. While the use of e-beam source and ozone has facilitated synthesizing epitaxial RuO₂ or other Ru-based oxides, they possess

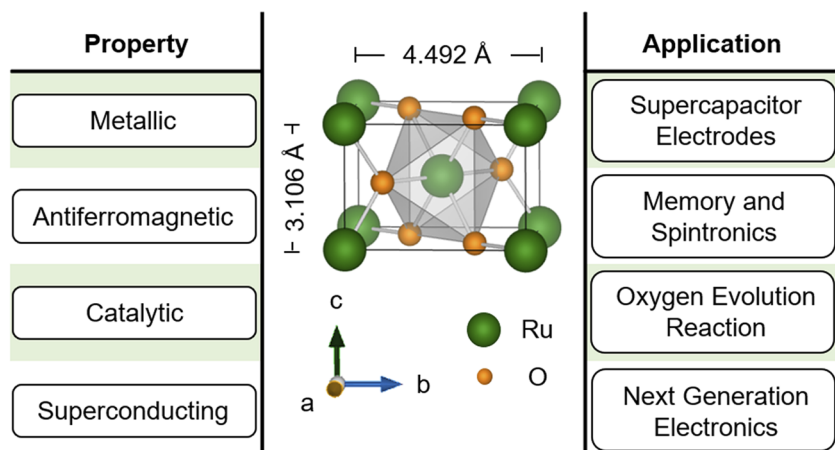


FIG. 1. Rutile crystal structure and lattice parameters for RuO_2 , a simple binary oxide, which exhibits many different property–application relationships.

several challenges associated with the issues related to the instability of fluxes and source oxidation in the presence of ozone.

In this paper, we demonstrate a novel solid-source metal–organic molecular beam epitaxy (MOMBE) approach using a detailed RuO_2 growth study that addresses these synthesis issues by using a solid metal–organic precursor as the metal Ru source.²⁵ This allows for supplying a “pre-oxidized” metal with order of magnitude higher vapor pressure than that of the elemental metal at a particular temperature.

II. EXPERIMENTAL SECTION

RuO_2 films were grown using the solid-source MOMBE approach, which has been described in more detail elsewhere.²⁵ Here, an effusion cell source temperature of 100°C was used for $\text{Ru}(\text{acac})_3$, and oxygen was supplied with a radio-frequency inductively coupled plasma source. An oxygen background pressure of $\sim 10^{-6}$ to 10^{-5} Torr was used. Substrate temperatures were 300°C , unless stated otherwise. Films were grown on *r*-plane sapphire $r\text{-Al}_2\text{O}_3$, TiO_2 (101), TiO_2 (110), TiO_2 (001), and TiO_2 (100) substrates.

Film surfaces were monitored before, during, and after growth using reflection high-energy electron diffraction (RHEED, Staib Instruments). Surface morphologies were imaged post growth using atomic force microscopy (AFM, Bruker). Structural characterization and determination of film thickness was carried out using high-resolution x-ray diffraction (HRXRD), reciprocal space mapping (RSM), and grazing incidence x-ray reflectivity (GIXR, Rigaku SmartLab XE). Thickness was also alternatively determined from finite thickness fringes if present in the HRXRD scans. X-ray photoelectron spectroscopy (XPS, Physical Electronics VersaProbe III) was used for determining the Ru oxidation state. Four-probe resistivity measurements were performed in the Van der Pauw geometry as a function of temperature (Quantum Design DynaCool Physical Property Measurement System). Ohmic contacts were made using aluminum wire bonds.

Cross-sectional Scanning Transmission Electron Microscopy (STEM) samples were prepared by a Focused Ion Beam (FIB) method using FEI Helios Nanolab G4 dual-beam FIB, where lamellae were cut and thinned using a 30 kV Ga-ion beam and further

polished with a 2 kV Ga-ion beam. Low-magnification high-angle annular dark-field STEM (HAADF-STEM) images were acquired using a Thermo Fischer Talos F200X, and atomic-resolution HAADF-STEM images and Energy Dispersive X-ray (EDX) elemental maps were obtained using an aberration-corrected FEI Titan G2 60-300 equipped with a super-X EDX detector. The microscopes were operated at 200 keV, and the screen current was ~ 25 pA. The probe semi-convergent angle was 10.5 and 17.3 mrad for Talos and Titan microscopes, respectively, and the detector angles for HAADF-STEM images were in the range of 55–110 mrad.

III. RESULTS AND DISCUSSION

Figure 2(a) shows the vapor pressure of Ru metal in comparison to that of the precursor used for Ru in this study, $\text{Ru}(\text{acac})_3$.²⁶ We also illustrate in Fig. 2(b) the important factors relevant to thin film synthesis by comparing them between e-beam-assisted MBE, hybrid MBE, and the solid-source MOMBE. Clearly, besides the advantages of high vapor pressure and the pre-oxidized state of the metal, the solid-source MOMBE also does not use a liquid precursor like hybrid MBE.²⁷ The solid metal–organic precursor can be sublimed in a conventional low temperature effusion cell directly in the vacuum system instead of a relatively complex gas inlet system. The low temperature effusion cell is also significantly less expensive, less complicated, and safer to operate than an e-beam source. The $\text{Ru}(\text{acac})_3$ precursor itself comes with an additional source of oxygen bonded in the ligands, is air stable, and is non-toxic, removing some safety concerns that can come with the use of metal–organic precursors, such as hexamethylditin (HMDT), in hybrid MBE growth of Sn-containing compounds.²⁸

Using the solid-source MOMBE approach, we first examined the effect of substrate temperature on the growth of RuO_2 . RuO_2 films were grown on $r\text{-Al}_2\text{O}_3$ with substrate temperatures (T_{sub}) from 300 to 850°C for a fixed growth time. All films were epitaxial and phase pure with a single peak corresponding to the RuO_2 (101) orientation, the common epitaxial orientation for rutile films on $r\text{-Al}_2\text{O}_3$, as shown in the HRXRD scans in Fig. 3(a).²⁹ As T_{sub} was increased, the growth rate increased, as shown in Fig. 3(b), which led to differences in the thickness of the films from 7 to 17 nm. As will be discussed later, the films grown at $T_{\text{sub}} = 750$ and 850°C had surfaces

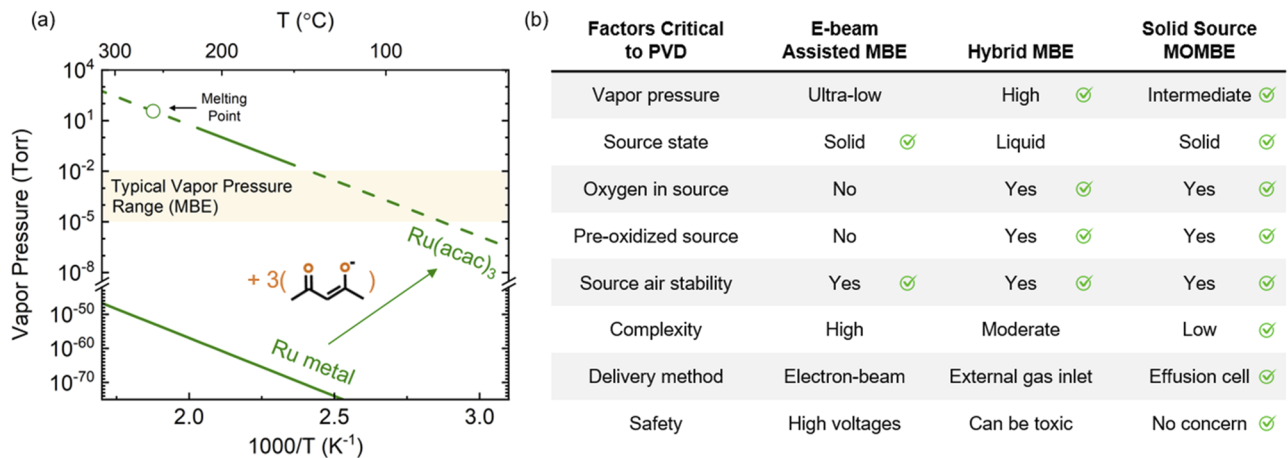


FIG. 2. (a) Vapor pressure of Ru metal and the metal-organic precursor, Ru(acac)₃. (b) Table of a few of the factors that are critical to the physical vapor deposition approaches, compared for electron-beam assisted MBE, hybrid MBE, and solid-source MOMBE. Green symbol signifies desirable.

too rough to determine a reliable thickness using GIXR. However, an estimate of the growth rates, and therefore thicknesses, is given in Fig. 3(b), obtained from the peak broadening of the (101) film peak using the Scherrer formula.³⁰ While the Scherrer analysis can give a poor approximation of the film thickness, thicknesses obtained here agreed well with those from GIXR and HRXRD thickness fringes for T ≥ 650 °C.

The initial increase and later saturation of the growth rate with increasing T_{sub} indicates a change of the growth mechanism from a reaction-limited to a flux-limited regime.³¹ This suggests that

below 650 °C, the growth rate is limited by the thermal decomposition of the Ru(acac)₃ precursor. Above 650 °C, the relatively constant growth rate is typical of being limited by the amount of precursor being supplied or the flux.³¹ No desorption-limited growth regime, i.e., a decrease in growth rate with increasing temperature, was observed. Nevertheless, the change from reaction- to flux-limited regime is not surprising and has been seen in other binary oxide systems grown by hybrid MBE approaches.^{29,32,33} Higher growth rates can be achieved by increasing Ru(acac)₃ precursor flux.

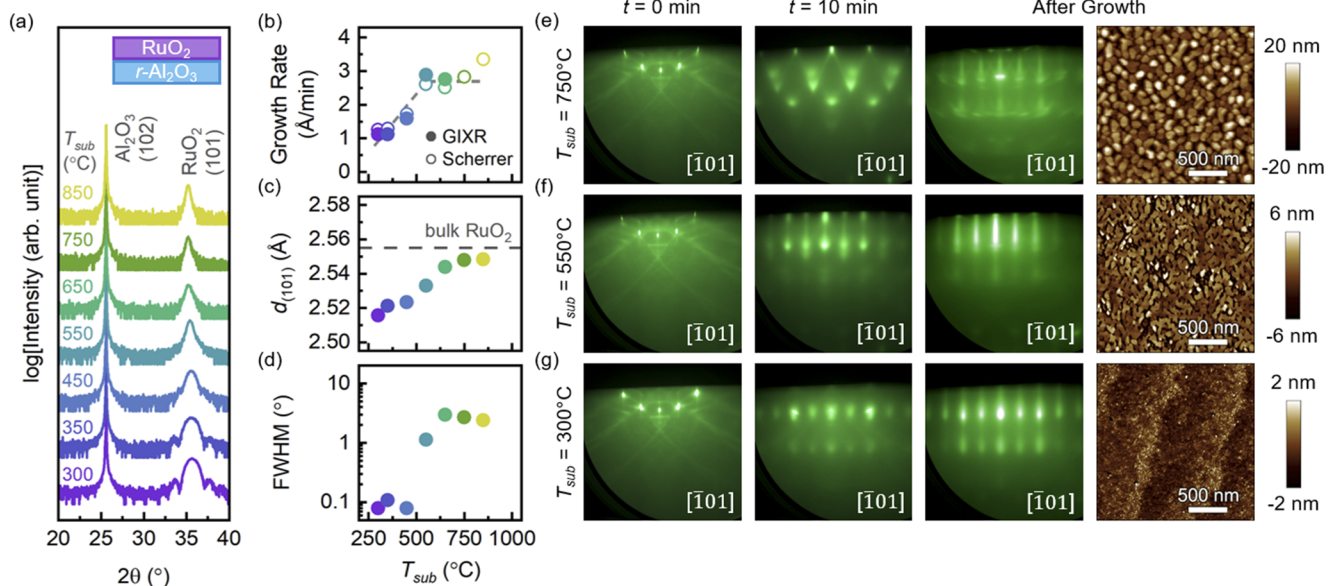


FIG. 3. (a) HRXRD patterns for RuO₂ (101) films grown on *r*-Al₂O₃ with increasing substrate temperature from bottom to top. (b) Growth rate, (c) out-of-plane (101) plane spacing, $d_{(101)}$, and (d) FWHM of the film (101) rocking curve peak. RHEED along the film $[\bar{1}01]$ azimuth taken before growth, 10 min into growth, and after growth along with post-growth AFM images for substrate temperatures of (e) 750 °C, (f) 550 °C, and (g) 300 °C.

With increasing T_{sub} , an increase in the out-of-plane spacing of (101) planes ($d_{(101)}$) was seen reaching toward the expected bulk value. The change in $d_{(101)}$ with T_{sub} is most likely due to the strain relaxation. To determine whether strain relaxation was due to the growth rate or film thickness, thicker films were grown at a constant growth rate by keeping $T_{sub} = 300$ °C (Fig. S1). In this case, even as thickness was increased up to 48 nm, $d_{(101)}$ did not reach the bulk value. For instance, a film thickness of 48 nm yielded $d_{(101)} = 2.538 \pm 0.002$ Å, which is significantly less than that of the 17 nm film ($d_{(101)} = 2.544 \pm 0.002$ Å) grown at higher temperatures (and at a higher growth rate). These results thus suggest that the strain relaxation is a more dominant effect at higher substrate temperatures, which is also accompanied by higher growth rates.

Consistent with strain relaxation with increasing temperature, the full width at half maximum (FWHM) of the film (101) rocking curves increased by about an order of magnitude from 450 to 550 °C, as shown in Fig. 3(d). RHEED images taken before growth, 10 min into growth, and after growth and cool down in oxygen (to $T_{sub} = 200$ °C), as well as the post-growth AFM images, are shown in Figs. 3(e), 3(f), and 3(g). From the AFM images, it can be clearly seen that the increase in FWHM was also accompanied by a roughening of the film surface. The difference in the surface morphologies was confirmed by RHEED to be a result of a change in the growth mode. At 10 min of growth, considerable differences in the RHEED patterns can be seen for these films grown at higher temperatures, with a change to an island growth mode. Irrespective of T_{sub} , XPS confirmed Ru^{4+} valence states in these samples (Fig. S2).

Having identified the optimal substrate temperatures of 300–450 °C, RuO_2 films were grown at 300 °C on TiO_2 substrates with different orientations. HRXRD scans, shown in Fig. 4(a), confirm phase pure, epitaxial, single crystalline films on all these substrates. Finite thickness fringes are present in all cases, although not very well defined in the case of TiO_2 (001), attesting to the high structural quality on a short lateral length scale. To investigate the structure of these films on an atomic scale, we performed STEM imaging of a representative RuO_2 film grown on TiO_2 (101) along $[\bar{1}01]$ and $[010]$ zone axes. Consistent with the HRXRD data, the phase pure, epitaxial film is seen with a sharp film/substrate interface with no misfit dislocations. The lack of dislocations signifies coherent growth, which agrees well with the strained $d_{101} = 2.51 \pm 0.002$ Å obtained from HRXRD. EDX elemental maps further attest to a uniform distribution of Ru in the film.

Interestingly, STEM images also reveal an atomically smooth surface along the $[010]$ zone axis, whereas a significantly rougher morphology was observed when viewed along the $[\bar{1}01]$ zone axis [Fig. 4(b)]. As shown in the zoomed-in image of Fig. 4(b), the rough surface was found to be terminated not only at the expected (101) plane parallel to the (101) TiO_2 substrate but also at the other plane consistent with the (111) face among others (Fig. S3). While the origin of this unusual surface morphology is unclear and remains a subject of future study, we argue that it may be related to the significantly different strain mismatches of +0.04% and +2.3% along $[\bar{1}01]$ and $[010]$ directions, respectively. While it is beyond the scope of this work, such a surface morphology will likely have an

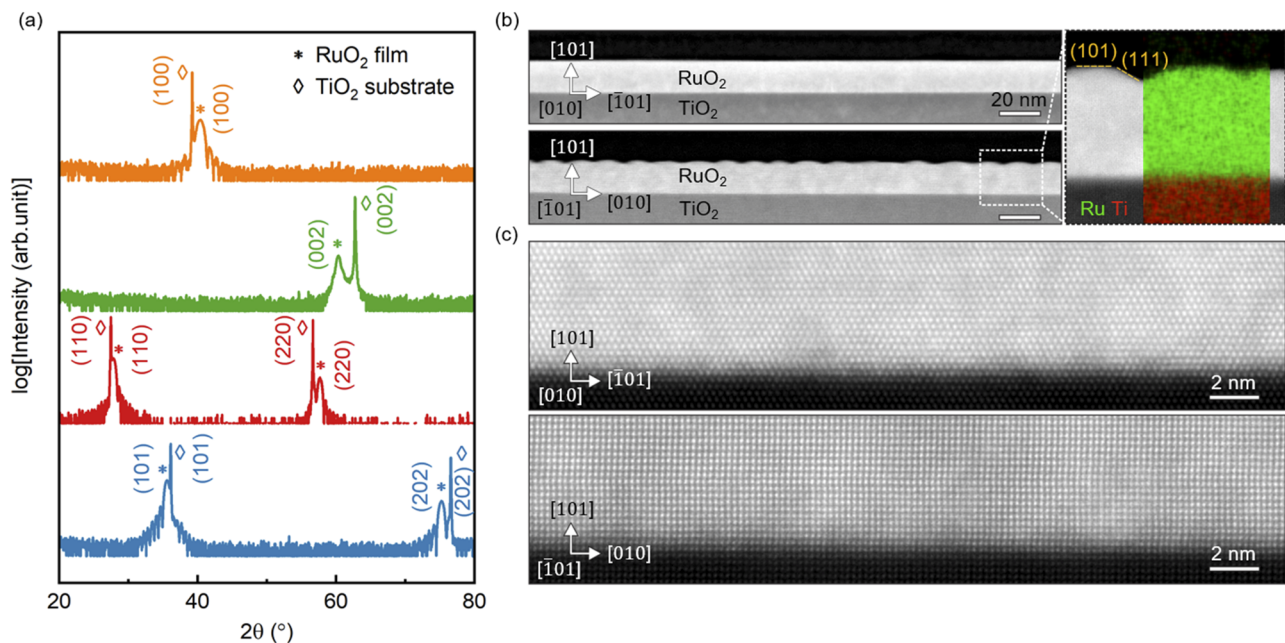


FIG. 4. (a) HRXRD patterns of RuO_2 films grown on a variety of TiO_2 substrate orientations: (101), (110), (001), and (100). Film thicknesses are 16, 12, 20, and 10 nm from bottom to top. (b) Cross-sectional HAADF-STEM images of 16 nm RuO_2 thin films grown on TiO_2 (101) in the $[010]$ and $[\bar{1}01]$ directions and STEM-EDX elemental map. The EDX map was constructed using $Ru L_{\alpha}$ and $Ti K_{\alpha}$ emissions. (c) Atomic-resolution HAADF-STEM images of the RuO_2/TiO_2 interface along the two different crystallographic orientations.

important implication on the oxygen evolution reaction using (101) RuO₂ films.

As a next step, we investigated the strain relaxation behavior of *t* nm RuO₂ film/TiO₂ (110) with *t* = 3–26 nm. Theoretically, RuO₂ on TiO₂ (110) has a relatively large lattice mismatch of about −4.7% and +2.3% along the [001] and [110] directions, respectively, indicating that coherently strained growth may be challenging on TiO₂ (110). Figure 5(a) shows HRXRD scans of *t* nm RuO₂ film/TiO₂ (110) with *t* = 3–26 nm revealing thickness fringes and film (110) peaks being partially overlapped with that of the substrate. The well-defined Kiessig fringes again attest to the high-quality film on a short lateral length scale. Upon analysis of the film peak position, 26 nm RuO₂ film/TiO₂ (110) yielded $d_{(110)} = 3.204 \pm 0.002$ Å, which is larger than the bulk value of 3.176 Å, suggesting partially strained films. To examine the strain state of these films along in-plane [001] and [110] directions, RSMs were taken. Figures 5(b)–5(e) show RSMs around (332) and (310) reflections for two representative films with *t* = 6 and 26 nm. As was expected, based on the value of $d_{(110)}$, the 26 nm sample was partially relaxed with both in-plane spacings, along the [001] and [110] directions, falling between the expected fully strained and fully relaxed values [Figs. 5(b) and 5(d)]. Interestingly, the 6 nm sample showed the same in-plane spacing as the 26 nm sample along the [001] direction (the [110] direction could not be determined due to overlap with the substrate) [Figs. 5(c) and 5(e)]. These results suggest that the strain relaxation begins to occur at *t* as small as 6 nm or less for the film grown on TiO₂ (110). Consistent with the strain relaxation behavior, a broadening of the (220) RuO₂ film rocking curve was seen with increasing *t*. Figures 5(f) and 5(g) show the rocking curves of 26 and 6 nm films, respectively. Rocking curves were fitted using two Gaussian peaks, marked as a broad and a narrow peak. The results of this fitting are shown in Figs. 5(h) and 5(i). Figure 5(h) shows that the narrow peak remained at a relatively constant FWHM of $\sim 0.07^\circ$, while the broad peak FWHM decreased with increasing

film thickness. Taking the ratio of the peak intensity of the broad component (I_{broad}) to the total intensity of the two ($I_{total} = I_{broad} + I_{narrow}$), Fig. 5(i), revealed an almost linear increase in this ratio with increasing film thickness. Results from the identical analysis of *t* nm RuO₂ film/*r*-Al₂O₃ are also included in Fig. 5(i), which compare well with films grown on TiO₂ (110) substrates.

The origin of the broad component can be thought of as being caused by the disorder induced due to the strain relaxation. We know that the strain relaxation process has begun by at least 6 nm based on the RSM results and likely at an even smaller thickness because of the presence of the broad component in the rocking curves of those films as well. As thickness is increased, the volume fraction of film that was influenced by the relaxation increases; therefore, the intensity of the broad component does as well. Similar results were seen in films grown on *r*-Al₂O₃, however, with a faster increase in the intensity ratio with increasing *t*. This observation is again consistent with faster strain relaxation expected from a larger lattice mismatch and difference in symmetry between RuO₂ and *r*-Al₂O₃.

Finally, we turn to the discussion of the electrical property of these films revealing a clear correlation between film thickness, strain relaxation, and electrical resistivity. Figure 6(a) shows the temperature-dependent resistivity (ρ) for *t* nm RuO₂ film/TiO₂ (110) with *t* = 3–15 nm. Films with *t* > 15 nm showed a large resistance anisotropy between the two in-plane directions for reliable four-terminal resistivity measurements, which is consistent with the prior results.¹⁰ All films showed metallic behavior with increasing resistivity with decreasing *t*. The room-temperature ρ of 15 nm was 55 $\mu\Omega$ cm, closest to the 35 $\mu\Omega$ cm of bulk RuO₂ among the films grown on TiO₂ (110).³⁴ Figure 6(b) shows the residual resistivities ($\rho_0 = \rho$ at 1.8 K) revealing an exponential-like decrease with increasing *t*, saturating at ~ 13 $\mu\Omega$ cm. Increasing film thickness can influence the electronic properties by way of finite size effects, such

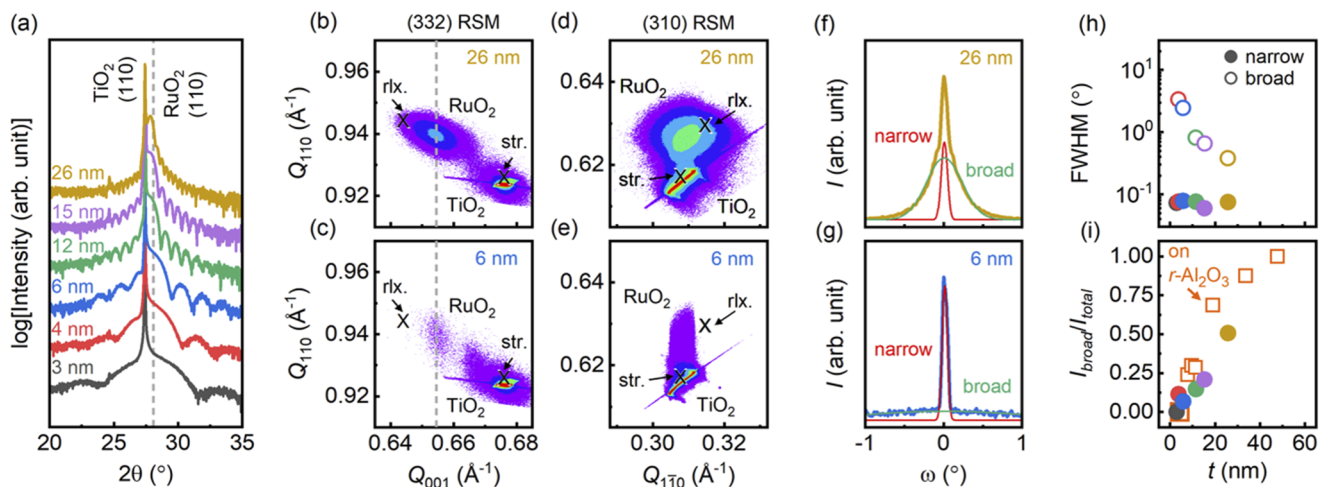


FIG. 5. (a) HRXRD patterns of RuO₂ films grown on TiO₂ (110) substrates with increasing thickness from bottom to top. (332) RSM for (b) 26 nm and (c) 6 nm films. (310) RSM for (d) 26 nm and (e) 6 nm films. Film (220) rocking curves for (f) 26 nm and (g) 6 nm films. Gaussian fits are shown for the “narrow” and “broad” peaks. In RSMs, str. and rlx. correspond to a fully strained and a fully relaxed position, respectively. Thickness-dependent (h) FWHM of the narrow and broad fits and (i) intensity ratio of broad peak intensity to total intensity for (220) film peaks.

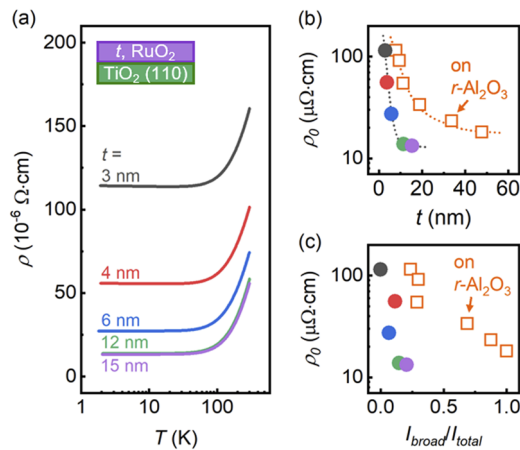


FIG. 6. (a) Resistivity (ρ) vs temperature for RuO₂ films grown on TiO₂ (110) as a function of film thickness. Residual resistivity (ρ_0), taken at 1.8 K, for RuO₂ grown on TiO₂ (110) (filled circles) and on *r*-Al₂O₃ (open squares) as a function of (b) film thickness and (c) intensity ratio of broad peak intensity to total intensity for (220) film peaks.

as effects from the film–substrate interface and dimensionality as well as the defects arising from the strain relaxation process, such as misfit and/or threading dislocations. With regard to the latter, as strain relaxation occurs and more defects are formed, the residual resistivity should likely increase as it is generally dependent on these structural crystalline defects. Here, we see the opposite trend, implying that the increase in thickness has a much larger effect on ρ than strain relaxation-related defect formation. To this end, we plot ρ_0 vs the film rocking curve intensity ratio we defined earlier in Fig. 6(c). This shows, once again, the opposite trend of what should be seen if strain relaxation was the critical factor. These data establish an important role of film dimensionality in the electrical transport properties of RuO₂ films.

IV. CONCLUSIONS

In summary, we have shown the growth of epitaxial RuO₂ films of different orientations using different substrates by a novel solid-source MOMBE. Single crystalline films with low film rocking curve FWHMs were grown on *r*-Al₂O₃ with substrate temperatures between 300 and 450 °C. At higher temperatures, films showed a significant increase in structural disorder. Using this approach and by keeping the substrate temperature at 300 °C, films were then grown on TiO₂ substrates with different orientations. STEM results confirmed phase pure, epitaxial films free of strain-relaxation-related defects when grown on TiO₂ (101). However, films on TiO₂ (110) were found to relax at thickness as low as 6 nm. Films with resistivity similar to that of the bulk RuO₂ single crystals were obtained for 15 nm RuO₂/TiO₂ (110). Finally, with increasing film thickness, we revealed an important role of film thickness on electrical properties. This work establishes the solid-source MOMBE technique for the growth of high-quality RuO₂ in a much simpler and cost-effective manner when compared to conventional MBE approaches. For instance, Ru metal was supplied by subliming a solid metal–organic precursor, Ru(acac)₃, in a low temperature effusion cell operating at

100 °C as opposed to several thousand using e-beam in conventional MBE.

SUPPLEMENTARY MATERIAL

See the [supplementary material](#) for HRXRD of RuO₂ films as a function of thickness and for the XPS revealing valence state of Ru.

AUTHORS' CONTRIBUTIONS

W.N. and S.N. grew samples. W.N., S.N., and A.K.M. performed HRXRD and AFM characterization. A.K.M. and A.R. performed temperature-dependent transport measurements. D.L. performed XPS measurements. H.Y. performed TEM sample preparation and STEM imaging under the guidance of K.A.M. W.N. and B.J. wrote the manuscript. All authors contributed to the discussion and manuscript preparation.

ACKNOWLEDGMENTS

This work was primarily supported by the U.S. Department of Energy through Grant No. DE-SC002021. The work also benefited from the Norwegian Centennial Chair Program (NOCC) and the Vannevar Bush Faculty Fellowship. S.N. and A.K.M. acknowledge support from the Air Force Office of Scientific Research (AFOSR) through Grant Nos. FA9550-19-1-0245 and FA9550-21-1-0025 and partially through NSF Grant No. DMR-1741801. D.L. acknowledges support from the U.S. DOE through the University of Minnesota Center for Quantum Materials under Award No. DE-SC0016371. A.R., H.Y., and K.A.M. acknowledge support from the UMN MRSEC program under Award No. DMR-2011401. Parts of this work were carried out at the Characterization Facility, University of Minnesota, which receives partial support from the NSF through the MRSEC program under Award No. DMR-2011401.

The authors declare no competing interests.

DATA AVAILABILITY

The data that support the findings of this study are available within the article and its [supplementary material](#) and from the corresponding author upon reasonable request.

REFERENCES

- M. Watanabe, M. Morishita, and Y. Ootuka, "Magnetoresistance of RuO₂-based resistance thermometers below 0.3 K," *Cryogenics* **41**(3), 143–148 (2001).
- Q. X. Jia, Z. Q. Shi, K. L. Jiao, W. A. Anderson, and F. M. Collins, "Reactively sputtered RuO₂ thin film resistor with near zero temperature coefficient of resistance," *Thin Solid Films* **196**(1), 29–34 (1991).
- L. Wang, C. Clavero, K. Yang, E. Radue, M. T. Simons, I. Novikova, and R. A. Lukaszew, "Bulk and surface plasmon polariton excitation in RuO₂ for low-loss plasmonic applications in NIR," *Opt. Express* **20**, 8618 (2012).
- F. Wang, S. Xiao, Y. Hou, C. Hu, L. Liu, and Y. Wu, "Electrode materials for aqueous asymmetric supercapacitors," *RSC Adv.* **3**(32), 13059–13084 (2013).
- C.-C. Hu, K.-H. Chang, M.-C. Lin, and Y.-T. Wu, "Design and tailoring of the nanotubular arrayed architecture of hydrous RuO₂ for next generation supercapacitors," *Nano Lett.* **6**(12), 2690–2695 (2006).
- J. Rossmel, Z. W. Qu, H. Zhu, G. J. Kroes, and J. K. Nørskov, "Electrolysis of water on oxide surfaces," *J. Electroanal. Chem.* **607**(1–2), 83–89 (2007).

- ⁷K. A. Stoerzinger, L. Qiao, M. D. Biegalski, and Y. Shao-Horn, "Orientation-dependent oxygen evolution activities of rutile IrO_2 and RuO_2 ," *J. Phys. Chem. Lett.* **5**(10), 1636–1641 (2014).
- ⁸D. Music, O. Kremer, G. Pernot, and J. M. Schneider, "Designing low thermal conductivity of RuO_2 for thermoelectric applications," *Appl. Phys. Lett.* **106**(6), 063906 (2015).
- ⁹D. Music, F. H.-U. Basse, L. Han, Devender, T. Borca-Tasciuc, J. J. Gengler, A. A. Voevodin, G. Ramanath, and J. M. Schneider, "Multifold Seebeck increase in RuO_2 films by quantum-guided lanthanide dilute alloying," *Appl. Phys. Lett.* **104**(5), 053903 (2014).
- ¹⁰J. P. Ruf, H. Paik, N. J. Schreiber, H. P. Nair, L. Miao, J. K. Kawasaki, J. N. Nelson, B. D. Faeth, Y. Lee, B. H. Goodge, B. Pamuk, C. J. Fennie, L. F. Kourkoutis, D. G. Schlom, and K. M. Shen, "Strain-stabilized superconductivity," *Nat. Commun.* **12**(1), 59 (2021).
- ¹¹M. Uchida, T. Nomoto, M. Musashi, R. Arita, and M. Kawasaki, "Superconductivity in uniquely strained RuO_2 films," *Phys. Rev. Lett.* **125**(14), 147001 (2020).
- ¹²T. Berlijn, P. C. Snijders, O. Delaire, H.-D. Zhou, T. A. Maier, H.-B. Cao, S.-X. Chi, M. Matsuda, Y. Wang, M. R. Koehler, P. R. C. Kent, and H. H. Weitering, "Itinerant antiferromagnetism in RuO_2 ," *Phys. Rev. Lett.* **118**(7), 077201 (2017).
- ¹³M. L. Green, M. E. Gross, L. E. Papa, K. J. Schnoes, and D. Brasen, "Chemical vapor deposition of ruthenium and ruthenium dioxide films," *J. Electrochem. Soc.* **132**(11), 2677 (1985).
- ¹⁴H. Maiwa, N. Ichinose, and K. Okazaki, "Preparation and properties of Ru and RuO_2 thin film electrodes for ferroelectric thin films," *Jpn. J. Appl. Phys., Part 1* **33**(9S), 5223 (1994).
- ¹⁵S. D. Bernstein, T. Y. Wong, Y. Kisler, and R. W. Tustison, "Fatigue of ferroelectric $\text{PbZr}_x\text{Ti}_{1-x}\text{O}_3$ capacitors with Ru and RuO_x electrodes," *J. Mater. Res.* **8**(1), 12–13 (1993).
- ¹⁶L. Krusin-Elbaum, M. Wittmer, and D. S. Yee, "Characterization of reactively sputtered ruthenium dioxide for very large scale integrated metallization," *Appl. Phys. Lett.* **50**(26), 1879–1881 (1987).
- ¹⁷E. Kolawa, F. C. T. So, W. Flick, X.-A. Zhao, E. T.-S. Pan, and M.-A. Nicolet, "Reactive sputtering of RuO_2 films," *Thin Solid Films* **173**(2), 217–224 (1989).
- ¹⁸Y. Gao, G. Bai, Y. Liang, G. C. Dunham, and S. A. Chambers, "Structure and surface morphology of highly conductive RuO_2 films grown on MgO by oxygen-plasma-assisted molecular beam epitaxy," *J. Mater. Res.* **12**(7), 1844–1849 (1997).
- ¹⁹D.-Y. Kuo, H. Paik, J. N. Nelson, K. M. Shen, D. G. Schlom, and J. Suntivich, "Chlorine evolution reaction electrocatalysis on RuO_2 (110) and IrO_2 (110) grown using molecular-beam epitaxy," *J. Chem. Phys.* **150**(4), 041726 (2019).
- ²⁰Y. J. Kim, Y. Gao, and S. A. Chambers, "Core-level X-ray photoelectron spectra and X-ray photoelectron diffraction of RuO_2 (110) grown by molecular beam epitaxy on TiO_2 (110)," *Appl. Surf. Sci.* **120**(3–4), 250–260 (1997).
- ²¹Q. Wang, W. L. Gladfelter, D. Fennell Evans, Y. Fan, and A. Franciosi, "Reactive-sputter deposition and structure of RuO_2 films on sapphire and strontium titanate," *J. Vac. Sci. Technol. A* **14**(3), 747–752 (1996).
- ²²G. Miao, A. Gupta, G. Xiao, and A. Anguelouch, "Epitaxial growth of ruthenium dioxide films by chemical vapor deposition and its comparison with similarly grown chromium dioxide films," *Thin Solid Films* **478**(1–2), 159–163 (2005).
- ²³Q. X. Jia, X. D. Wu, S. R. Foltyn, A. T. Findikoglu, P. Tiwari, J. P. Zheng, and T. R. Jow, "Heteroepitaxial growth of highly conductive metal oxide RuO_2 thin films by pulsed laser deposition," *Appl. Phys. Lett.* **67**(12), 1677–1679 (1995).
- ²⁴Q. X. Jia, S. G. Song, X. D. Wu, J. H. Cho, S. R. Foltyn, A. T. Findikoglu, and J. L. Smith, "Epitaxial growth of highly conductive RuO_2 thin films on (100) Si," *Appl. Phys. Lett.* **68**(8), 1069–1071 (1996).
- ²⁵W. Nunn, A. K. Manjeshwar, J. Yue, A. Rajapitamahuni, T. K. Truttman, and B. Jalan, "Novel synthesis approach for 'stubborn' metals and metal oxides," *Proc. Natl. Acad. Sci. U. S. A.* **118**, e2105713118 (2021).
- ²⁶J. R. Rumble, *CRC Handbook of Chemistry and Physics* (CRC Press; Taylor & Francis Group, Boca Raton, FL, 2020), Vol. 101.
- ²⁷B. Jalan, R. Engel-Herbert, N. J. Wright, and S. Stemmer, "Growth of high-quality SrTiO_3 films using a hybrid molecular beam epitaxy approach," *J. Vac. Sci. Technol. A* **27**(3), 461–464 (2009).
- ²⁸A. Prakash, J. Dewey, H. Yun, J. S. Jeong, K. A. Mkhoyan, and B. Jalan, "Hybrid molecular beam epitaxy for the growth of stoichiometric BaSnO_3 ," *J. Vac. Sci. Technol. A* **33**(6), 060608 (2015).
- ²⁹B. Jalan, R. Engel-Herbert, J. Cagnon, and S. Stemmer, "Growth modes in metal-organic molecular beam epitaxy of TiO_2 on *r*-plane sapphire," *J. Vac. Sci. Technol. A* **27**(2), 230–233 (2009).
- ³⁰P. Scherrer, "Bestimmung der inneren struktur und der gröÙe von kolloidteilchen mittels röntgenstrahlen," in *Kolloidchemie Ein Lehrbuch* (Springer, 1912), pp. 387–409.
- ³¹C. J. Taylor, D. C. Gilmer, D. G. Colombo, G. D. Wilk, S. A. Campbell, J. Roberts, and W. L. Gladfelter, "Does chemistry really matter in the chemical vapor deposition of titanium dioxide? Precursor and kinetic effects on the microstructure of polycrystalline films," *J. Am. Chem. Soc.* **121**(22), 5220–5229 (1999).
- ³²T. Wang, A. Prakash, E. Warner, W. L. Gladfelter, and B. Jalan, "Molecular beam epitaxy growth of SnO_2 using a tin chemical precursor," *J. Vac. Sci. Technol. A* **33**(2), 020606 (2015).
- ³³A. Prakash, T. Wang, R. Choudhary, G. Haugstad, W. L. Gladfelter, and B. Jalan, "Precursor selection in hybrid molecular beam epitaxy of alkaline-earth stannates," *J. Vac. Sci. Technol. A* **38**, 063410 (2020).
- ³⁴W. D. Ryden, A. W. Lawson, and C. C. Sartain, "Electrical transport properties of IrO_2 and RuO_2 ," *Phys. Rev. B* **1**(4), 1494 (1970).